AGU ADVANCING EARTH AND SPACE SCIENCE

Geophysical Research Letters

RESEARCH LETTER
10.1029/2022GL101692

# Constraining Fault Damage Zone Properties From Geodesy: A Case Study Near the 2019 Ridgecrest Earthquake Sequence

**Xiaohua Xu[1,2], Dunyu Liu[2], and Luc Lavier[2]**

[1]University of Science and Technology of China, Hefei, Chaina, [2]Institute for Geophysics, University of Texas at Austin, Austin, TX, USA

**Key Points:**

- We developed a geodetic modeling approach to constrain structural and mechanical properties of fault damage zones
- The approach is straightforward, computationally efficient, and works well even over a small fault damage zone with 250 m width
- The existence of many shallow fractures indicates distributed shallow strain release over transtensional shear zones

**Supporting Information:**

Supporting Information may be found in the online version of this article.

**Correspondence to:**

X. Xu,
xiaohua-xu@ustc.edu.cn

**Citation:**

Xu, X., Liu, D., & Lavier, L. (2023). Constraining fault damage zone properties from geodesy: A case study near the 2019 Ridgecrest earthquake sequence. *Geophysical Research Letters*, *50*, e2022GL101692. https://doi.org/10.1029/2022GL101692

Received 11 OCT 2022
Accepted 12 FEB 2023

**Author Contributions:**

**Conceptualization:** Xiaohua Xu, Luc Lavier
**Data curation:** Xiaohua Xu
**Formal analysis:** Xiaohua Xu
**Investigation:** Xiaohua Xu, Dunyu Liu, Luc Lavier
**Methodology:** Xiaohua Xu
**Resources:** Xiaohua Xu
**Software:** Xiaohua Xu, Dunyu Liu
**Supervision:** Luc Lavier
**Validation:** Xiaohua Xu
**Visualization:** Xiaohua Xu
**Writing – original draft:** Xiaohua Xu
**Writing – review & editing:** Xiaohua Xu, Dunyu Liu, Luc Lavier



**Abstract** Seismologic studies have reported seismic velocities reduction and $V_p/V_s$ ratio changes over damage zones associated with seismogenic faults. The structure and elastic properties of these damage zones indicate the maturity of faults and affect the rupture dynamics of future seismic events. Therefore, they contain critical information about fault properties that could inform seismic hazards. Here we present a geodetic modeling approach to constrain velocity changes and elastic properties of fault damage zones under stress perturbation from nearby earthquakes. Compared to seismic tomographic analysis that is usually limited by resolution, this geodetic approach provides tighter constraints on the elastic properties and geometry of the damage zone at shallow depths. Our results imply that a major component of the shallow strain release is distributed and inelastic. The existence of numerous shallow faults either may indicate a locally detached shallow layer or they are remnants from earlier fault evolution.

**Plain Language Summary** Ruptures of large earthquakes tend to fracture the materials nearby, thus creating a zone with lower seismic velocity, which is known as fault damage zone. Understanding the structure and mechanics of this zone will help reveal the status of fault evolution and seismogenic depth for future ruptures. To achieve that, we developed a geodetic modeling approach to determine the geometric and physical parameters of fault damage zones, utilizing observations from high-resolution Interferometric Synthetic Aperture Radar and strain release estimates from kinematic fault slip models. By searching the parameters in a specific order, each unknown could be uniquely constrained from the observed deformation profiles. The approach works well with fault damage zones under compliant motion induced by the stress from nearby earthquakes. The method is straightforward, computationally efficient and is applicable even to a fault damage zone with 250 m width near the 2019 Ridgecrest earthquake sequence. Our study suggests that these structures are quite shallow and accommodate a major component of shallow strain release.

## 1. Introduction

Strike-slip faults are surrounded by a zone of highly deformed wall rocks that are associated with a network of secondary faults and cracks (Chester & Logan, 1986; Martel & Boger, 1998; Woodcock & Fischer, 1986). The development of this damage zone usually correlates with fault length growth and accumulation of slip (Cowie & Scholz, 1992; Manighetti et al., 2007, 2009; McGrath & Davison, 1995; Savage & Brodsky, 2011). The enhanced complexity of stress distribution due to the existence of such zones tend to dynamically affect earthquake nucleation and rupture propagation (Huang & Ampuero, 2011; Ma & Elbanna, 2015; Thakur et al., 2020; Weng et al., 2016). Prior studies have suggested reduced seismic velocities in fault damage zones ranging from 20% to 60% (Allam & Ben-Zion, 2012; Ben-Zion et al., 2003; Lewis & Ben-Zion, 2010; Li et al., 1990, 1998; Lu & Ben-Zion, 2022; Qiu et al., 2021; Vidale & Li, 2003; Zhou et al., 2022), and changes in Vp/Vs ratio up to 10% (Jiang et al., 2021; Zhang et al., 2009). These reduced velocities may drop further by a few percentage points with strong passing seismic waves and heal over the following months to decades (Li et al., 2006, 1998; Vidale & Li, 2003). Mechanically, fault damage zones with seismic velocity reductions are equivalent to an elastic zone with reduced moduli (Shearer, 2019). Strain accumulation or release associated with the fault damage zones could be measured from crustal deformation (Barbot et al., 2009; Lindsey et al., 2014; Materna & Bürgmann, 2016). Furthermore, when a fault damage zone experiences large stress perturbations caused by nearby earthquakes, the reduced elastic moduli will notably increase the magnitude of deformation in the damage zone compared to the host rock and causes high strain in the form of compliant fault deformation (Cochran et al., 2009; Fialko et al., 2002, Hamiel & Fialko, 2007; Xu, Sandwell, & Smith-Konter, 2020; Xu, Sandwell, Ward, et al., 2020). Xu, Sandwell, Ward, et al. (2020) shows that this type of compliant deformation

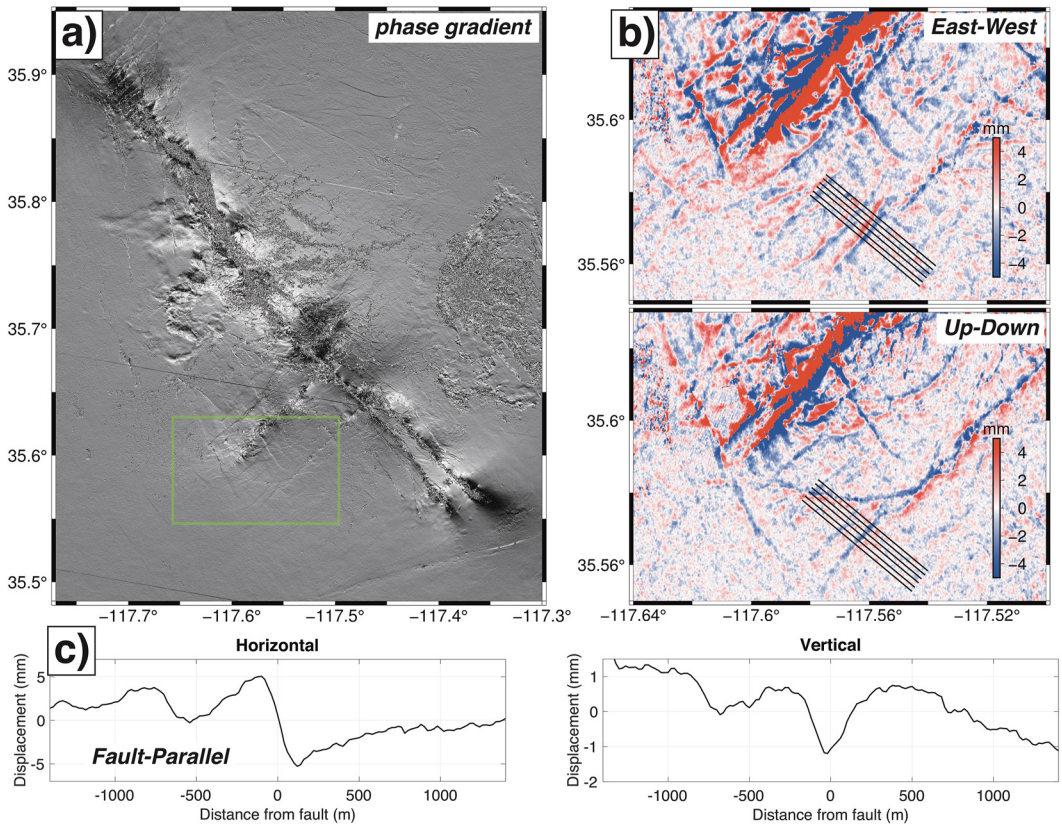


**Figure 1.** Displacement across a compliant fault damage zone near the 2019 Ridgecrest earthquake sequence from Xu, Sandwell, and Smith-Konter (2020) and Xu, Sandwell, Ward, et al. (2020). (a) Azimuthal phase gradient measurement from Sentinel-1 Interferometric Synthetic Aperture Radar (InSAR) data, from which a large number of fractures and faults are identified. The green box denotes the area plotted in (b). (b) Plots of high-pass filtered decomposed displacement along east-west (top) and up-down (bottom) directions. The black solid lines represent the paths along which displacements are taken and stacked in (c). (c) Plots of stacked fault-parallel and vertical displacements across the chosen compliant fault damage zone. A trend is removed to make the amplitude symmetric on both sides of the fault and no filtering is applied to these profiles. The profile is chosen based on field investigations that confirmed no brittle fracture.

only exists when the stress perturbation is in the opposite direction to the tectonic stress loading. The faults driven forward (in alignment to tectonic stress) are likely to slip frictionally, while those driven backward will be under compliant motion within fault damage zones. This duality indicates all shallow faults loaded by tectonic stress are on the verge of moving forward, thus creating a buffer for compliant motions when external stress drives the faults backward. To further understand the spatial variability and temporal evolution of this phenomenon, it is necessary to quantify the structure of fault zones and their seismic velocity changes. To achieve that goal, we develop a geodetic-modeling approach to determine the structural and mechanical properties of fault damage zones under stress perturbations from nearby large earthquakes. The high-quality geodetic observations from modern Interferometric Synthetic Aperture Radar (InSAR) are the most critical element in the approach.

The approach requires knowledge of the displacements over the compliant fault and strain release from nearby source earthquake. We use profiles derived from InSAR acquisitions from the Sentinel-1 satellites (Torres et al., 2012) operated by the European Space Agency (Figure 1). The level of shear and extensional strain (Figure 2a) over the fault damage zone are estimated using a kinematic slip model inverted using InSAR, optical and GNSS data (Xu, Sandwell, Ward, et al., 2020), with forward calculations done using Okada's elastic half-space model (Okada, 1992). With these known inputs above, the unknowns, or our targets, are the fault damage zone width, depth, and the modulus ratio for the materials in and outside of the fault damage zone. Below we discuss in detail how our approach connects the knowns (Section 2) with the unknowns (Section 3) using a 3D finite element model (FEM) of the deformation across a compliant elastic fault damage zone.

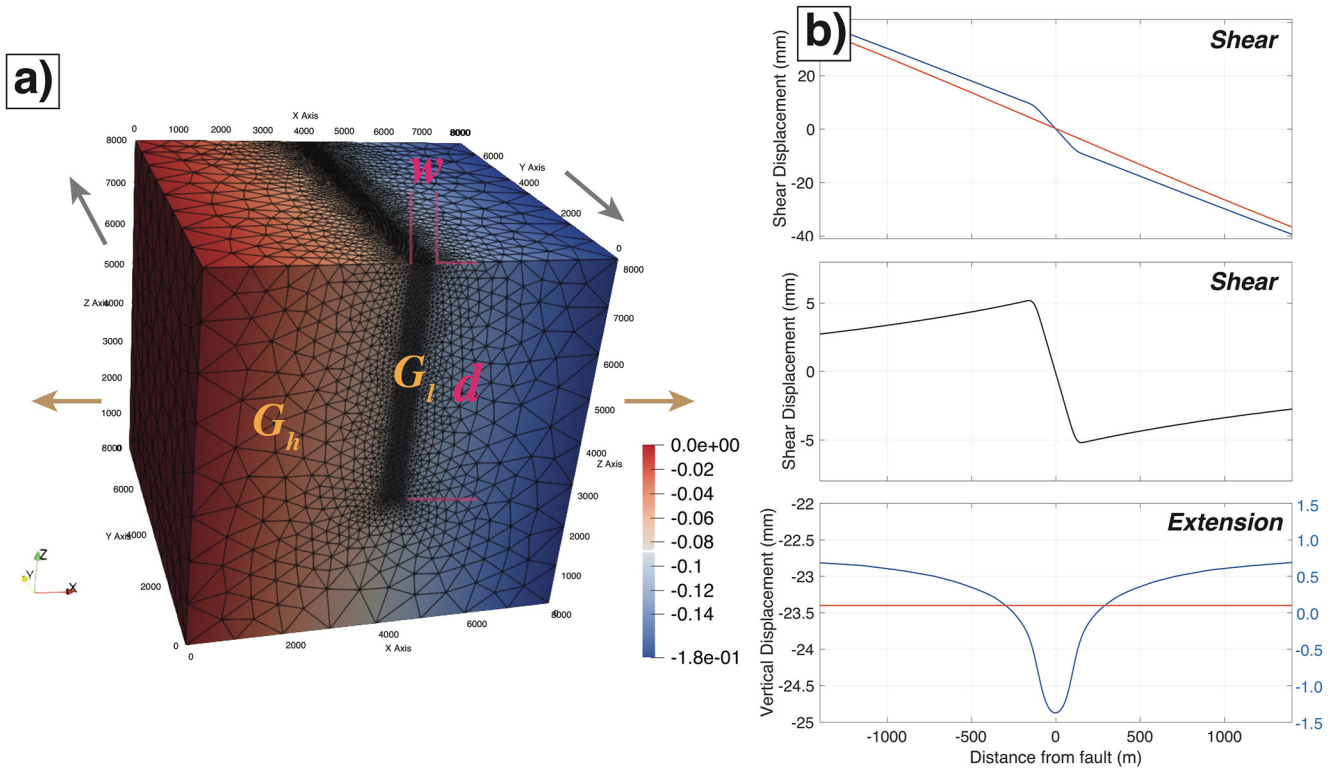


**Figure 2.** Finite element model setup for analysis of the compliant deformation across a fault damage zone buried in a homogeneous media. (a) The sketch of the model mesh generated by *Gmsh* with background solution computed by *FEniCS* and visualized in *paraview*. The pink letters denote the structural parameters of a box-shaped fault damage zone (width and depth), and the orange letters are the shear modulus for the hosting rock ($G_h$) and the fault damage zone ($G_l$). (b) Plots of the shear displacement (top), detrended shear displacement (middle, blue-red in (a)), and vertical displacement (bottom) along distance from fault. Red and blue curves are for scenario of homogeneous model and model with a fault damage zone. The axis on the right-hand side for the bottom plot shows the value of the blue curve after subtracting the red curve.

## 2. Geodetic Observations and Slip Model

On July 4 and 5, 2019, just 6 hr apart, two earthquakes with *Mw* 6.4 and *Mw* 7.1 struck Ridgecrest California, US (USGS, 2019a, 2019b). The two earthquakes took place on conjugate faults near the Airport Lake and the Little Lake fault zones (Ross et al., 2019), and induced localized strain over hundreds of fractures nearby (Xu, Sandwell, Ward, et al., 2020). The rupture and detailed deformation from this earthquake sequence were well imaged by the twin Sentinel-1 satellites (Xu, Sandwell, & Smith-Konter, 2020). The InSAR data were processed with pure geometric coregistration (Sansosti, 2006; Xu et al., 2017), and stacked to reduce noise. A phase-gradient approach (Sandwell & Price, 1998) was incorporated to detect small changes on the nearby structures (Figure 1a), where bright or dark linear fractures indicate deformation over short spatial scales. We decomposed the InSAR data from descending and ascending orbits to get decomposed east-west and up-down components, taking advantage of the look angles along the satellite line-of-sight (LOS) being largely symmetric from the two tracks. Then the decomposed data were high-pass filtered for illustration purposes (Figure 1b), thus the sense of motion over the fractures could be determined. We took profiles over one of the retrograde fractures (i.e., in the opposite sense of motion to the rupture) on the unfiltered data and removed trend to level the amplitude of deformation across the fracture (Figure 1c). The horizontal and vertical profiles both show continuum of shear and subsidence which is consistent with the definition of compliant fault deformation over a fault damage zone (Segall, 2010). More details on this part of analysis are documented in Xu, Sandwell, & Smith-Konter (2020) and Xu, Sandwell, Ward, et al. (2020).

To further analyze the strain conditions of this specific fault damage zone, we utilized a kinematic slip model from a prior study by Xu, Sandwell, Ward, et al. (2020). The model is constructed incorporating geodetic observations from InSAR LOS displacements from both Sentinel-1 and ALOS-2 (Rosenqvist et al., 2014) data, multi-aperture interferometry data, optical imagery cross-correlation (Milliner & Donnellan, 2020), and GNSS offsets from

Scripps Orbit and Permanent Array Center (SOPAC). The Green's function used in the inversion is an analytical solution in elastic half-space (Okada, 1985), and then the kinematic slip model is forwarded to predict the strain components over the damage zone (Okada, 1992).

## 3. Method and Finite Element Modeling

To get an initial set up for the later FEM (Figure 2), we first derive the mathematical formulation to calculate elastic modulus reduction from InSAR measurements. We calculate the shear modulus reduction in an assumed fault damage zone throughout the model depth over elastic half-space. Assuming a half-space homogeneous media (with shear modulus $G_h$) is subjected to shear stress change $\Delta\sigma_t$, the relation with shear displacement $dx$ across the fault damage zone with width $w$ (Figure 2b, top red) can be written as

$$\frac{2dxG_h}{w} = \Delta\sigma_t \tag{1}$$

Similarly, for a half-space embedded with a top-to-bottom fault damage zone that has reduced shear modulus $G_l$, the displacement $dx'$ across the damage zone (Figure 2b, top blue) can then be written similarly as

$$\frac{2dx'G_l}{w} = \Delta\sigma_t \tag{2}$$

Then the residual shear displacement (Figure 2b, middle), or the differential amount across the fault can be estimated as

$$dx' - dx = w\Delta\sigma_t\left(\frac{1}{2G_l} - \frac{1}{2G_h}\right) \tag{3}$$

and the ratio of shear moduli can be derived as

$$\frac{G_l}{G_h} = \frac{1}{\frac{2(dx'-dx)G_h}{w\Delta\sigma_t} + 1} = \frac{1}{\frac{dx'-dx}{w\varepsilon_t} + 1} \tag{4}$$

where $\varepsilon_t$ is the shear strain over the homogeneous media that can be predicted by a kinematic slip model using the analytical solution for elastic half-space (Okada, 1985, 1992). Note that Equation 4 is independent of the absolute value of shear modulus and requires no estimate of actual stress changes. For the specific case shown in Figure 1c, with the estimated shear strain being 22.0E−06, and 10.3 mm displacement across a 250 m fault damage zone, the resulting shear modulus ratio is ~0.35 which corresponds to ~40% reduction in shear wave velocity.

Next, we search the parameter space of the FEM to generate the compliant fault deformation that fit the geodetic measurements. We use *FEniCS*, an open-source computing platform for solving partial differential equations (Alnæs et al., 2015) for the finite element modeling. We generate the mesh using *Gmsh* (Geuzaine & Remacle, 2009), an open-source mesh generator, with a 250-m fault damage zone hosted in an 8-km (32 times the width) sized box (Figure 2a). The width of the damage zone is directly measured from the horizontal profile (Figure 1c) by differentiating the positions of maximum displacement. Do note the simulated deformation profile produces the same width as the fault zone width in the model setup. The boundary conditions of the model ensure that the strain matches the estimates from the kinematic slip model (i.e., $22.0 \times 10^{-6}$ shear and $11.7 \times 10^{-6}$ extension). Indeed, these estimates rely on the validity of assumed elasticity and simplified geometry, yet as long as the model fits surface displacements, the derived strain field should remain largely the same. We validate the performance of the simulation by comparing the determined shear modulus from modeling to the estimated value using Equation 4 (Figure S1 in Supporting Information S1). The best matching shear modulus ratio 0.33 (for 5 km depth), which produces the exact amplitude of shear displacement, is in close agreement with the value estimated above (0.35). The minor difference could be due to that our model setup has a limited depth for the fault damage zone.

We then search the three-parameter space, that is, damage zone depth, shear modulus ratio, and Poisson's ratio, to determine the solution that best fit the measured horizontal and vertical deformation profiles. The three parameters have different effects on the deformation, and we explore them in a certain order. The first parameter,

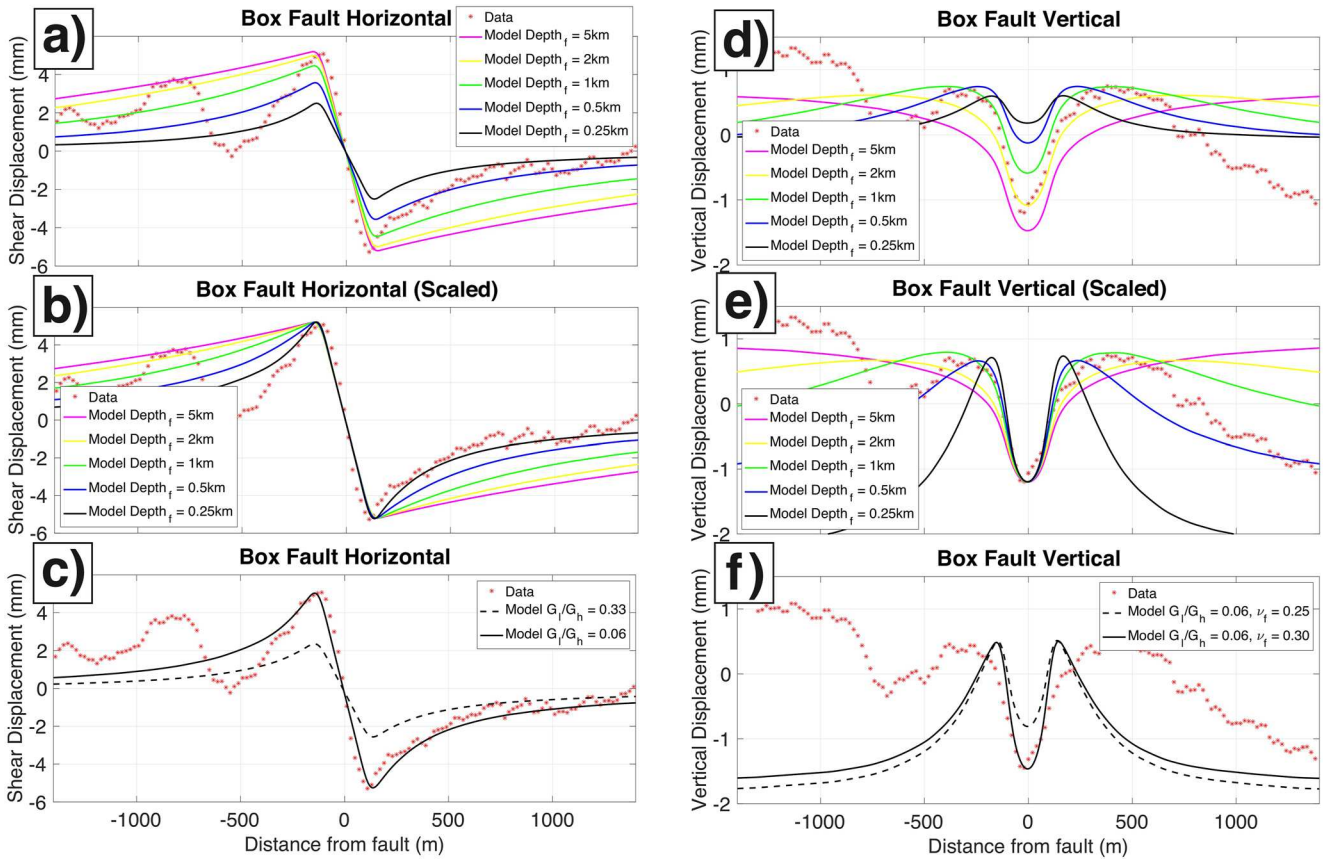


**Figure 3.** Simulation on the deformation profiles across a 250 m wide fault damage zone using *FEniCS*. (a) Plotted shear displacement when changing the depth of fault damage zone (0.25–5 km) given shear modulus ratio of 0.33. (b) Same as (a) except the amplitude is scaled to match the total displacement across the fault. (c) Shear displacement when changing the shear modulus ratio from 0.33 to 0.06, where the dashed curve is the same as the black curve in (a). (d) Plotted vertical displacement when changing the depth of fault damage zone, similar to (a), with shear modulus ratio being 0.33. (e) Scaled version of (d) to match the amplitude of subsidence across the fault. (f) Vertical displacement when changing the Poisson's ratio given fixed shear modulus, where the dashed curve is with depth 0.25 km and the shear modulus ratio is 0.06.

fault damage zone depth, generally produces two effects on the shear and vertical deformation curves (Figures 3a and 3d). A shallower depth will introduce a smaller amplitude in both shear and subsidence, and more importantly attenuates the compliant deformation outside the damage zone at a faster rate over distance from fault. The unique control from the fault damage zone depth parameter is the attenuation of the shear curves, in the sense that a smaller buried heterogeneity will bring the deformation faster to the homogeneous model. Thus, by scaling the amplitude of the curves with different depth setups (i.e., bring up the amplitude to the same level), one could easily determine which one produces the correct decay (Figure 3b), that is 0.25 km for this model setup. The shear modulus ratio controls the displacement amplitude (Figure 3c). Larger displacement is expected with weaker fault damage zone. For this case, the best matching shear modulus ratio is 0.06. With the two parameters determined, we adjust the Poisson's ratio inside the fault damage zone to fit the amplitude of vertical displacement. By increasing the Poisson's ratio in the damage zone to 0.3 (hosting rock remains 0.25), more subsidence is achieved. The increased Poisson's ratio corresponds to an 8% increase in Vp/Vs ratio, which finds its support from seismic tomography studies over fault damage zones (Jiang et al., 2021; Zhang et al., 2009).

Now we have acquired the structural and mechanical parameters of the fault damage zone, yet the underlying assumption is that this damage zone is in a box-shape. We then further explore the possibility of a V-shaped damage zone that approximates the flower structure (Figure S2 in Supporting Information S1). The change in shape yields faster decay on deformation amplitude and outside the damage zone, which is mainly due to the smaller volume of the V-shape compared to a box fault given the same width and depth (Figure S3 in Supporting Information S1). Again, we found the best matching depth to be about 0.25 km. However, this particular depth is unable to produce enough shear no matter how small of a shear modulus is given (Figure S3c in Supporting

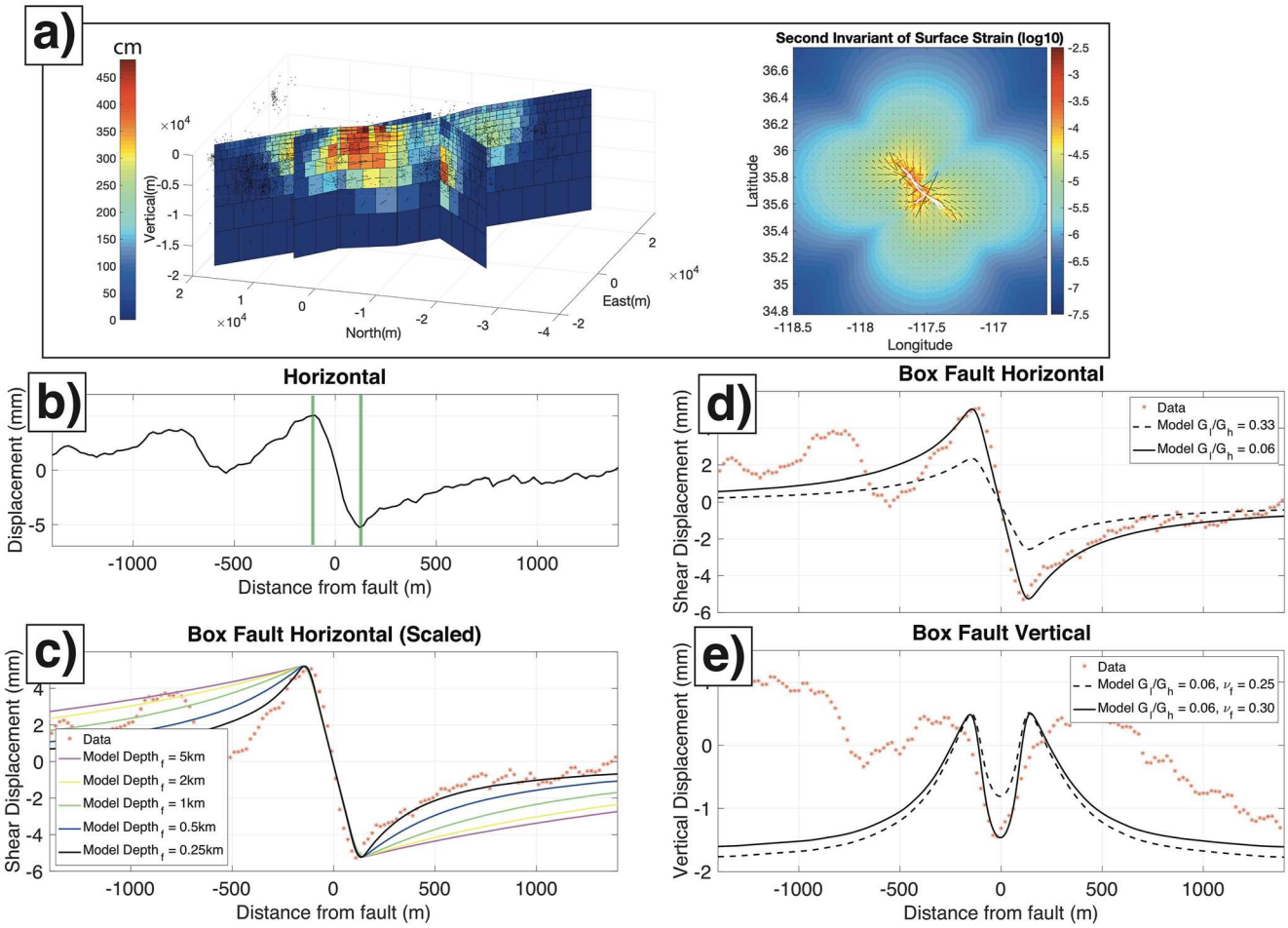


**Figure 4.** Summary of the approach to get geodetic constraint for the structural and mechanical parameters of a fault damage zone. (a) Left plot is the kinematic slip model from Xu, Sandwell, Ward, et al. (2020), with the plot on the right being the derived surface strain. (b) Horizontal displacement profile, same as Figure 1c, where width of the fault damage zone could be directly measured. (c) Scaled shear displacement with changing depths of the fault damage zone, same as Figure 3b, where based on how well they are matching, one could determine the depth extent of the damage zone. (d) Shear displacement when changing the shear modulus ratio, same as Figure 3c, with which one could determine the best value to match the displacement amplitude. (e) Vertical displacement when changing p-wave velocity (or Poisson's ratio), same as Figure 3f, where one can find the best value to match the amplitude of vertical displacement over the damage zone.

Information S1). Thus, we chose a slightly larger depth of 0.5 km for the 250 m wide V-shaped damage zone scenario, and the resulting shear modulus ratio is 0.12 (Figure S3d in Supporting Information S1) with Poisson' ratio being 0.27 (Figure S3g in Supporting Information S1) for the fault damage zone. Indeed, from this analysis, a trade-off between fault damage zone depth and shear modulus ratio is posted, in order to produce the right amount of displacement. Yet similar problem does not exist for the box-shaped scenario, which may indicate the reality being a box fault damage zone or maybe a combination of the two.

The approach can be summarized as below:

1. Gather InSAR observations of a large earthquake and identify compliant deformation over faults in the vicinity of the rupture, by combining phase and phase-gradient maps (Xu, Sandwell, & Smith-Konter, 2020). Decompose the observations into east-west and up-down directions, stack profiles along the target fault to reduce noise (Figure 1c), and project the horizontal into fault-parallel direction.
2. Invert for a kinematic slip model using all available geodetic data (Xu et al., 2016), and calculate strain over the target fault damage zone (Okada, 1992) (Figure 4a).
3. Measure the fault damage zone width directly from horizontal displacement curves (Figure 4b).
4. Construct an FEM to simulate the compliant deformation over the fault damage zone, and by comparing the decay of deformation outside the fault damage zone, determine the proper depth for the fault damage zone (Figure 4c).

5. Change shear modulus ratio to get the right amount of shear (Figure 4d).
6. Fix fault depth and shear modulus ratio and change the Poisson's ratio in the fault damage zone, so that the model produce the exact amount of vertical displacement (Figure 4e).

## 4. Discussion and Implications

The case of compliant fault deformation we adopted here is a common one among all the retrograde faults near Ridgecrest (Xu, Sandwell, Ward, et al., 2020). The resulting shear modulus (0.06) from our analysis on this specific fault damage zone indicate a 75% shear wave velocity reduction. Likely, this number is larger than most reported seismic studies near Ridgecrest (Lu & Ben-Zion, 2022; Qiu et al., 2021; Zhou et al., 2022). However, considering this zone is at shallowest surface layer at a transtensional boundary (Oldow et al., 1994), this value could be indicative and meaningful, especially considering that static rigidity is generally lower than dynamic rigidity (Ciccotti & Mulargia, 2004; Eissa & Kazi, 1988). Similar analyses discussed above are essentially applicable to the vertical deformation as well, albeit we seek only to target the vertical amplitude, not the shape of the profile for this specific case, mainly due to the much smaller subsidence (1/6) compared to the shear (Figures 4d and 4e).

The approach above arguably is for a fault damage zone under ideal conditions, where both localized horizontal and vertical deformation are observed. In reality, due to the variety of orientations and properties of the existing faults, the two types of deformation may not always be available. With strong horizontal but no vertical measurement, our approach could resolve the shear modulus ratio and fault damage zone depth as in step 1–5. With only vertical available, one may have to estimate a fault damage zone width and depth based on the simulation (Figures 3d and 3e), and then acquire proper shear modulus ratio that yield proper vertical amplitude. If the satellite observation only allows one measurement along LOS, where no decomposed components along east-west and up-down are available, one will have to search a set of fault depth, width, and shear modulus ratio simultaneously as was done in earlier studies (Fialko et al., 2002; Hamiel & Fialko, 2007; Hearn & Fialko, 2009). However, the latter case should be rare with the constellation of modern satellites such as Sentinel-1 and ALOS-2.

We note that the arbitrary detrending on displacement profiles may affect the estimates of the structural and mechanical parameters, especially on the depth extent of the damage zone. If an extra slope is imposed on the current detrended data, the best curve will not fit the data as well as before. However, this does not grant a better fitting to the curves with other parameters, in the sense that the decay outside the damage zone is nonlinear and known to approach zero at far end (Figure 2b). One could make an assessment on the uncertainties of parameters by evaluating the misfit to the displacement data, yet existence of noise and other fractures may cause strong bias to the estimates. The best fitting model shows a slightly under-predicted shear displacement toward the edge of the damage zone, though the total magnitude of shear matches observations well (Figure 3c). This under-prediction essentially indicates the strain localization, or in other words, reduction of shear modulus or damage, is stronger toward the fault core. Our estimated moduli reduction, at least for this specific case, is an averaged effect over the fault damage zone.

Our approach provides an independent geodetic constraint on structural and mechanical parameters of fault damage zones without requiring further assumptions or assistance from other instruments. The computation is relatively light. The InSAR processing with the GMTSAR software (Sandwell et al., 2016) and kinematic slip modeling (Xu et al., 2016) are accessible with a common 4-core and 16G-memory laptop. Particularly, the simulation with *FEniCS* only takes a few minutes to run even with the largest depth extent we put in the model. Currently, the approach works with faults under compliant deformation and requires strong stress perturbation, such as an earthquake nearby, both of which may not be often available simultaneously. Another limitation is that the approach is mainly sensitive to the shallowest depths (Figure 3b). Once the fault damage zone depth goes larger than 10 times the damage zone width, the displacement curves are barely differentiable from a damage zone beyond.

Prior studies have shown that the widths of the damage zones generally reflect the depth extent of the seismogenic faults (Ampuero & Mao, 2017). Though out of the exact scope of the analyzed depths in the prior simulations, a very shallow depth range can be inferred for the specific case presented, and the damage zones over these nearby faults around Ridgecrest can be considered as an endmember for the proposed approach. In scenarios of much more mature and wider fault damage zones (Dolan & Haravitch, 2014; Savage & Brodsky, 2011), the expected

displacement under the same stress perturbation should be much larger and detectable with the high-quality InSAR observations from the modern (e.g., Sentinel-1 and ALOS-2) and future (e.g., NISAR) SAR missions.

From a macroscopic view, these faults or fractures have an increased density toward the major rupture, the distribution of which follows a power law (Rodriguez Padilla, Oskin, et al., 2022). A large fraction of them is within the damage zone of the ruptured fault, as is captured by aerial imagery (Pierce et al., 2020; Rodriguez Padilla, Quintana, et al., 2022), with the rest hosted on shallow and distributed structures, which is resolved by InSAR (Xu, Sandwell, & Smith-Konter, 2020). Although the two types can be fit into the same distribution, their characteristics are completely different. Both could be candidate hypothesis to explain the reduced shallow rupture over many large strike slip earthquakes, that is, the shallow slip deficit (Fialko et al., 2005; Kaneko & Fialko, 2011; Simons et al., 2002; Xu et al., 2016). For those that are similar to the case presented, due to their shallow depth extent, they are not expected to continuously slip over many earthquake cycles, as that will introduce large amount of strain at the bottom of the structure. Thus, this poses us a dilemma: either the shallowest layer of the Earth can be locally detached from the hosting rock momentarily due to shaking or fluid, that is, it could accumulate and release strain inelastically on its own; or these structures get deeper into the seismogenic depth but only exist for a period of time. The former implies existence of a brittle sedimentary layer that under the shear from the hosting rock beneath, develops such distributed fractures and essentially their distribution should follow the level of strain accumulation as a power law (i.e., derivative of displacement for a locked fault, $\arctan(x)' = 1/(1+x^2)$). For two-dimensional density of a planar fault, a square root is expected for this relationship, and this argument is supported by measured fracture density over fault-perpendicular distance near Ridgecrest (Rodriguez Padilla, Oskin, et al., 2022). However, whether this hypothesis prevails needs verification on their depth extent from imaging tools, such as seismic arrays or Distributed Acoustic Sensing (Atterholt et al., 2022; Yang et al., 2022), and further evidence over other shear zones, as it may be just limited to the transtensional regime near Ridgecrest. The latter on the other hand implies that these structures occur at early stage of fault development and gets fossilized as the crustal strain gets localized toward the major fault. As the strain gets centered toward the actual fault plane, the level of maximum strain over an earthquake cycle on these structures drops with time and seldom will they slip again, though their shallow-most parts still respond to the stress perturbation from nearby large earthquakes. Most of such structures near Ridgecrest has total length from a few to tens of kilometers, and corresponding to the displacement-length scaling, they should have only slipped tens to hundreds of meters over time (Cowie & Scholz, 1992). Compared to other more mature faults at Eastern California, for example, Roadman (Dokka & Travis, 1990) and Calico (Oskin et al., 2007) that have around 10 km accumulated slip, these structures are indeed immature. Nonetheless, the implication from both hypotheses is that a major component of the shallow strain release is distributed and inelastic.

## 5. Conclusions

We developed an approach to determine structural and mechanical parameters for compliant fault damage zones under stress perturbation from nearby large earthquakes. The approach is straightforward, computationally efficient, and works well on even the tiniest fault structures near Ridgecrest. Such analysis is made possible primarily by the enhanced quality of radar data acquired by modern constellation of InSAR satellites. The approach also relies on well-developed numerical tools like GMTSAR, kinematic fault slip model and finite element code developed with FEniCS. Our case study utilizes data over a very thin damage zone which ensures the applicability to more mature faults with wider damage zones. It also reveals the shallow depth extent and strong damage level for the compliant fault near Ridgecrest. The existence of large number of such shallow secondary faults near Ridgecrest, despite of their formation mechanism, implies distributed and inelastic shallow strain release either present or in the past.

## Data Availability Statement

All data are originally available through the Copernicus Open Access Hub (https://scihub.copernicus.eu), Alaska Data Search (https://search.asf.alaska.edu), and SOPAC (http://sopac-csrc.ucsd.edu). Kinematic inversion results are available at a Dryad repository corresponding to Xu, Sandwell, Ward, et al. (2020) (https://doi.org/10.5061/dryad.18931zcxg) and is done using the Geodetic Inversion Package available on GitHub (https://github.com/Xiaohua-Eric-Xu/Geodetic_Inversion_Package_with_Matlab). The Finite Element Modeling

is done using *FEniCS* (https://github.com/FEniCS) and *Gmsh*, with scripts available on GitHub (https://github.com/dunyuliu/Compliant_deformation_over_fault_damage_zone).

**Acknowledgments**
The authors want to thank Alba M. Rodriguez Padilla and Dezheng Zhao for their valuable suggestions that significantly improved this manuscript. We also want to thank European Space Agency for the extraordinary data open policy on the Sentinel-1 mission and want to thank Alaska Satellite Facility for archiving the data and the precise orbital products. This study was funded by the National Science Fundation (NSF) Cyberinfrastructure for Sustained Scientific Innovation (CSSI) program (2209807) and the Southern California Earthquake Center (SCEC) (22020). SCEC is funded by the NSF cooperative Agreement EAR-1033462 and USGS Cooperative Agreement G12AC20038.

## References

Allam, A. A., & Ben-Zion, Y. (2012). Seismic velocity structures in the southern California plate-boundary environment from double-difference tomography. *Geophysical Journal International*, *190*(2), 1181–1196. https://doi.org/10.1111/j.1365-246x.2012.05544.x

Alnæs, M., Blechta, J., Hake, J., Johansson, A., Kehlet, B., Logg, A., et al. (2015). The FEniCS project version 1.5. *Archive of Numerical Software*, *3*(100). https://doi.org/10.11588/ans.2015.100.20553

Ampuero, J., & Mao, X. (2017). Upper limit on damage zone thickness controlled by seismogenic depth. In *Fault zone dynamic processes: Evolution of fault properties during seismic rupture* (Vol. 227, pp. 243–253). American Geophysical Union (Chap. 13).

Atterholt, J., Zhan, Z., & Yang, Y. (2022). Fault zone imaging with distributed acoustic sensing: Body-to-surface wave scattering. *Journal of Geophysical Research: Solid Earth*, *127*(11), e2022JB025052.

Barbot, S., Fialko, Y., & Sandwell, D. (2009). Three-dimensional models of elastostatic deformation in heterogeneous media, with applications to the Eastern California Shear Zone. *Geophysical Journal International*, *179*(1), 500–520. https://doi.org/10.1111/j.1365-246x.2009.04194.x

Ben-Zion, Y., Peng, Z., Okaya, D., Seeber, L., Armbruster, J. G., Ozer, N., et al. (2003). A shallow fault-zone structure illuminated by trapped waves in the Karadere–Duzce branch of the North Anatolian Fault, western Turkey. *Geophysical Journal International*, *152*(3), 699–717.

Chester, F. M., & Logan, J. M. (1986). Implications for mechanical properties of brittle faults from observations of the Punchbowl fault zone, California. *Pure and Applied Geophysics*, *124*(1), 79–106. https://doi.org/10.1007/bf00875720

Ciccotti, M., & Mulargia, F. (2004). Differences between static and dynamic elastic moduli of a typical seismogenic rock. *Geophysical Journal International*, *157*(1), 474–477. https://doi.org/10.1111/j.1365-246x.2004.02213.x

Cochran, E. S., Li, Y. G., Shearer, P. M., Barbot, S., Fialko, Y., & Vidale, J. E. (2009). Seismic and geodetic evidence for extensive, long-lived fault damage zones. *Geology*, *37*(4), 315–318. https://doi.org/10.1130/g25306a.1

Cowie, P. A., & Scholz, C. H. (1992). Displacement-length scaling relationship for faults: Data synthesis and discussion. *Journal of Structural Geology*, *14*(10), 1149–1156. https://doi.org/10.1016/0191-8141(92)90066-6

Dokka, R. K., & Travis, C. J. (1990). Role of the eastern California shear zone in accommodating Pacific-North American plate motion. *Geophysical Research Letters*, *17*(9), 1323–1326. https://doi.org/10.1029/gl017i009p01323

Dolan, J. F., & Haravitch, B. D. (2014). How well do surface slip measurements track slip at depth in large strike-slip earthquakes? The importance of fault structural maturity in controlling on-fault slip versus off-fault surface deformation. *Earth and Planetary Science Letters*, *388*, 38–47. https://doi.org/10.1016/j.epsl.2013.11.043

Eissa, E. A., & Kazi, A. (1988). Relation between static and dynamic Young's moduli of rocks. *International Journal of Rock Mechanics and Mining & Geomechanics Abstracts*, *25*(6), 479–482. https://doi.org/10.1016/0148-9062(88)90987-4

Fialko, Y., Sandwell, D., Agnew, D., Simons, M., Shearer, P., & Minster, B. (2002). Deformation on nearby faults induced by the 1999 Hector Mine earthquake. *Science*, *297*(5588), 1858–1862. https://doi.org/10.1126/science.1074671

Fialko, Y., Sandwell, D., Simons, M., & Rosen, P. (2005). Three-dimensional deformation caused by the Bam, Iran, earthquake and the origin of shallow slip deficit. *Nature*, *435*(7040), 295–299. https://doi.org/10.1038/nature03425

Geuzaine, C., & Remacle, J. F. (2009). Gmsh: A 3-D finite element mesh generator with built-in pre-and post-processing facilities. *International Journal for Numerical Methods in Engineering*, *79*(11), 1309–1331. https://doi.org/10.1002/nme.2579

Hamiel, Y., & Fialko, Y. (2007). Structure and mechanical properties of faults in the North Anatolian Fault system from InSAR observations of coseismic deformation due to the 1999 Izmit (Turkey) earthquake. *Journal of Geophysical Research*, *112*(B7), B07412. https://doi.org/10.1029/2006jb004777

Hearn, E. H., & Fialko, Y. (2009). Can compliant fault zones be used to measure absolute stresses in the upper crust? *Journal of Geophysical Research*, *114*(B4), B04403. https://doi.org/10.1029/2008jb005901

Huang, Y., & Ampuero, J. P. (2011). Pulse-like ruptures induced by low-velocity fault zones. *Journal of Geophysical Research*, *116*(B12), B12307. https://doi.org/10.1029/2011jb008684

Jiang, X., Hu, S., & Yang, H. (2021). Depth extent and Vp/Vs ratio of the Chenghai Fault Zone, Yunnan, China constrained from dense-array-based teleseismic receiver functions. *Journal of Geophysical Research: Solid Earth*, *126*(8), e2021JB022190. https://doi.org/10.1029/2021JB022190

Kaneko, Y., & Fialko, Y. (2011). Shallow slip deficit due to large strike-slip earthquakes in dynamic rupture simulations with elasto-plastic off-fault response. *Geophysical Journal International*, *186*(3), 1389–1403. https://doi.org/10.1111/j.1365-246x.2011.05117.x

Lewis, M. A., & Ben-Zion, Y. (2010). Diversity of fault zone damage and trapping structures in the Parkfield section of the San Andreas Fault from comprehensive analysis of near fault seismograms. *Geophysical Journal International*, *183*(3), 1579–1595. https://doi.org/10.1111/j.1365-246x.2010.04816.x

Li, Y. G., Chen, P., Cochran, E. S., Vidale, J. E., & Burdette, T. (2006). Seismic evidence for rock damage and healing on the San Andreas fault associated with the 2004 M 6.0 Parkfield earthquake. *Bulletin of the Seismological Society of America*, *96*(4B), S349–S363. https://doi.org/10.1785/0120050803

Li, Y. G., Leary, P., Aki, K., & Malin, P. (1990). Seismic trapped modes in the Oroville and San Andreas fault zones. *Science*, *249*(4970), 763–766. https://doi.org/10.1126/science.249.4970.763

Li, Y. G., Vidale, J. E., Aki, K., Xu, F., & Burdette, T. (1998). Evidence of shallow fault zone strengthening after the 1992 M 7.5 Landers, California, earthquake. *Science*, *279*(5348), 217–219. https://doi.org/10.1126/science.279.5348.217

Lindsey, E. O., Fialko, Y., Bock, Y., Sandwell, D. T., & Bilham, R. (2014). Localized and distributed creep along the southern San Andreas fault. *Journal of Geophysical Research: Solid Earth*, *119*(10), 7909–7922. https://doi.org/10.1002/2014jb011275

Lu, Y., & Ben-Zion, Y. (2022). Regional seismic velocity changes following the 2019 Mw 7.1 Ridgecrest, California earthquake from autocorrelations and P/S converted waves. *Geophysical Journal International*, *228*(1), 620–630. https://doi.org/10.1093/gji/ggab350

Ma, X., & Elbanna, A. E. (2015). Effect of off-fault low-velocity elastic inclusions on supershear rupture dynamics. *Geophysical Journal International*, *203*(1), 664–677. https://doi.org/10.1093/gji/ggv302

Manighetti, I., Campillo, M., Bouley, S., & Cotton, F. (2007). Earthquake scaling, fault segmentation, and structural maturity. *Earth and Planetary Science Letters*, *253*(3–4), 429–438. https://doi.org/10.1016/j.epsl.2006.11.004

Manighetti, I., Zigone, D., Campillo, M., & Cotton, F. (2009). Self-similarity of the largest-scale segmentation of the faults: Implications for earthquake behavior. *Earth and Planetary Science Letters*, *288*(3–4), 370–381. https://doi.org/10.1016/j.epsl.2009.09.040

Martel, S. J., & Boger, W. A. (1998). Geometry and mechanics of secondary fracturing around small three-dimensional faults in granitic rock. *Journal of Geophysical Research*, *103*(B9), 21299–21314. https://doi.org/10.1029/98jb01393

Materna, K., & Bürgmann, R. (2016). Contrasts in compliant fault zone properties inferred from geodetic measurements in the San Francisco Bay area. *Journal of Geophysical Research: Solid Earth*, *121*(9), 6916–6931. https://doi.org/10.1002/2016jb013243

McGrath, A. G., & Davison, I. (1995). Damage zone geometry around fault tips. *Journal of Structural Geology*, *17*(7), 1011–1024. https://doi.org/10.1016/0191-8141(94)00116-h

Milliner, C., & Donnellan, A. (2020). Using daily observations from Planet Labs satellite imagery to separate the surface deformation between the 4 July Mw 6.4 foreshock and 5 July Mw 7.1 mainshock during the 2019 Ridgecrest earthquake sequence. *Seismological Research Letters*, *91*(4), 1986–1997. https://doi.org/10.1785/0220190271

Okada, Y. (1985). Surface deformation due to shear and tensile faults in a half-space. *Bulletin of the Seismological Society of America*, *75*(4), 1135–1154. https://doi.org/10.1785/bssa0750041135

Okada, Y. (1992). Internal deformation due to shear and tensile faults in a half-space. *Bulletin of the Seismological Society of America*, *82*(2), 1018–1040. https://doi.org/10.1785/bssa0820021018

Oldow, J. S., Kohler, G., & Donelick, R. A. (1994). Late Cenozoic extensional transfer in the Walker Lane strike-slip belt, Nevada. *Geology*, *22*(7), 637–640. https://doi.org/10.1130/0091-7613(1994)022<0637:lcetit>2.3.co;2

Oskin, M., Perg, L., Blumentritt, D., Mukhopadhyay, S., & Iriondo, A. (2007). Slip rate of the Calico fault: Implications for geologic versus geodetic rate discrepancy in the Eastern California Shear Zone. *Journal of Geophysical Research*, *112*(B3), B03402. https://doi.org/10.1029/2006jb004451

Pierce, I., Williams, A., Koehler, R. D., & Chupik, C. (2020). High-resolution structure-from-motion models and orthophotos of the southern sections of the 2019 Mw 7.1 and 6.4 Ridgecrest earthquakes surface ruptures. *Seismological Research Letters*, *91*(4), 2124–2126. https://doi.org/10.1785/0220190289

Qiu, H., Ben-Zion, Y., Catchings, R., Goldman, M. R., Allam, A. A., & Steidl, J. (2021). Seismic imaging of the Mw 7.1 Ridgecrest earthquake rupture zone from data recorded by dense linear arrays. *Journal of Geophysical Research: Solid Earth*, *126*(7), e2021JB022043. https://doi.org/10.1029/2021jb022043

Rodriguez Padilla, A. M., Oskin, M. E., Milliner, C. W., & Plesch, A. (2022). Accrual of widespread rock damage from the 2019 Ridgecrest earthquakes. *Nature Geoscience*, *15*(3), 222–226. https://doi.org/10.1038/s41561-021-00888-w

Rodriguez Padilla, A. M., Quintana, M. A., Prado, R. M., Aguilar, B. J., Shea, T. A., Oskin, M. E., & Garcia, L. (2022). Near-field high-resolution maps of the Ridgecrest earthquakes from aerial imagery. *Seismological Society of America*, *93*(1), 494–499. https://doi.org/10.1785/0220210234

Rosenqvist, A., Shimada, M., Suzuki, S., Ohgushi, F., Tadono, T., Watanabe, M., et al. (2014). Operational performance of the ALOS global systematic acquisition strategy and observation plans for ALOS-2 PALSAR-2. *Remote Sensing of Environment*, *155*, 3–12. https://doi.org/10.1016/j.rse.2014.04.011

Ross, Z. E., Idini, B., Jia, Z., Stephenson, O. L., Zhong, M., Wang, X., et al. (2019). Hierarchical interlocked orthogonal faulting in the 2019 Ridgecrest earthquake sequence. *Science*, *366*(6463), 346–351. https://doi.org/10.1126/science.aaz0109

Sandwell, D. T., & Price, E. J. (1998). Phase gradient approach to stacking interferograms. *Journal of Geophysical Research*, *103*(B12), 30183–30204. https://doi.org/10.1029/1998jb900008

Sandwell, D. T., Xu, X., Mellors, R., Wei, M., Tong, X., & Wessel, P. (2016). GMTSAR: An InSAR processing system based on generic mapping tools (2nd ed.). Retrieved from http://topex.ucsd.edu/gmtsar/tar/GMTSAR_2ND_TEX.pdf

Sansosti, E., Berardino, P., Manunta, M., Serafino, F., & Fornaro, G. (2006). Geometrical SAR image registration. *IEEE Transactions on Geoscience and Remote Sensing*, *44*(10), 2861–2870. https://doi.org/10.1109/tgrs.2006.875787

Savage, H. M., & Brodsky, E. E. (2011). Collateral damage: Evolution with displacement of fracture distribution and secondary fault strands in fault damage zones. *Journal of Geophysical Research*, *116*(B3), B03405. https://doi.org/10.1029/2010jb007665

Segall, P. (2010). Earthquake and volcano deformation. In *Earthquake and volcano deformation* (pp. 120–125). Princeton University Press.

Shearer, P. M. (2019). *Introduction to seismology* (p. 32). Cambridge University Press.

Simons, M., Fialko, Y., & Rivera, L. (2002). Coseismic deformation from the 1999 Mw 7.1 Hector Mine, California, earthquake as inferred from InSAR and GPS observations. *Bulletin of the Seismological Society of America*, *92*(4), 1390–1402. https://doi.org/10.1785/0120000933

Thakur, P., Huang, Y., & Kaneko, Y. (2020). Effects of low-velocity fault damage zones on long-term earthquake behaviors on mature strike-slip faults. *Journal of Geophysical Research: Solid Earth*, *125*(8), e2020JB019587. https://doi.org/10.1029/2020jb019587

Torres, R., Snoeij, P., Geudtner, D., Bibby, D., Davidson, M., Attema, E., et al. (2012). GMES Sentinel-1 mission. *Remote Sensing of Environment*, *120*, 9–24. https://doi.org/10.1016/j.rse.2011.05.028

U.S. Geological Survey (USGS). (2019a). Event page "M 7.1 – 2019 Ridgecrest earthquake sequence". Retrieved from https://earthquake.usgs.gov/earthquakes/eventpage/ci38457511/executive (last accessed December 2019).

U.S. Geological Survey (USGS). (2019b). Event page "M 6.4 – 11 km SW of Searles valley, CA". Retrieved from https://earthquake.usgs.gov/earthquakes/eventpage/ci38443183/executive (last accessed December 2019).

Vidale, J. E., & Li, Y. G. (2003). Damage to the shallow Landers fault from the nearby Hector Mine earthquake. *Nature*, *421*(6922), 524–526. https://doi.org/10.1038/nature01354

Weng, H., Yang, H., Zhang, Z., & Chen, X. (2016). Earthquake rupture extents and coseismic slips promoted by damaged fault zones. *Journal of Geophysical Research: Solid Earth*, *121*(6), 4446–4457. https://doi.org/10.1002/2015jb012713

Woodcock, N. H., & Fischer, M. (1986). Strike-slip duplexes. *Journal of Structural Geology*, *8*(7), 725–735. https://doi.org/10.1016/0191-8141(86)90021-0

Xu, X., Sandwell, D. T., & Smith-Konter, B. (2020). Coseismic displacements and surface fractures from Sentinel-1 InSAR: 2019 Ridgecrest earthquakes. *Seismological Research Letters*, *91*(4), 1979–1985. https://doi.org/10.1785/0220190275

Xu, X., Sandwell, D. T., Tymofyeyeva, E., Gonzalez-Ortega, A., & Tong, X. (2017). Tectonic and anthropogenic deformation at the Cerro Prieto geothermal step-over revealed by Sentinel-1A InSAR. *IEEE Transactions on Geoscience and Remote Sensing*, *55*(9), 5284–5292. https://doi.org/10.1109/tgrs.2017.2704593

Xu, X., Sandwell, D. T., Ward, L. A., Milliner, C. W., Smith-Konter, B. R., Fang, P., & Bock, Y. (2020). Surface deformation associated with fractures near the 2019 Ridgecrest earthquake sequence. *Science*, *370*(6516), 605–608. https://doi.org/10.1126/science.abd1690

Xu, X., Tong, X., Sandwell, D. T., Milliner, C. W., Dolan, J. F., Hollingsworth, J., et al. (2016). Refining the shallow slip deficit. *Geophysical Journal International*, *204*(3), 1867–1886. https://doi.org/10.1093/gji/ggv563

Yang, Y., Zhan, Z., Shen, Z., & Atterholt, J. (2022). Fault zone imaging with distributed acoustic sensing: Surface-to-surface wave scattering. *Journal of Geophysical Research: Solid Earth*, *127*(6), e2022JB024329. https://doi.org/10.1029/2022jb024329

Zhang, H., Thurber, C., & Bedrosian, P. (2009). Joint inversion for Vp, Vs, and Vp/Vs at SAFOD, Parkfield, California. *Geochemistry, Geophysics, Geosystems*, *10*(11). https://doi.org/10.1029/2009gc002709

Zhou, Z., Bianco, M., Gerstoft, P., & Olsen, K. (2022). High-resolution imaging of complex shallow fault zones along the July 2019 Ridgecrest ruptures. *Geophysical Research Letters*, *49*(1), e2021GL095024. https://doi.org/10.1029/2021gl095024